Femtosecond Direct Space-to-Time Pulse Shaping

Daniel E. Leaird and Andrew M. Weiner, *Fellow, IEEE*

***Abstract*—The direct space-to-time (DST) pulse shaping apparatus is investigated both theoretically and experimentally. The discussion shows how the operation of the DST pulse shaper may be understood in terms of the femtosecond response of a generalized spectrometer. A complete discussion of the advantages and tradeoffs of utilizing this pulse-shaping configuration is given, including the direct scaling between the masking function and the output temporal intensity profile, system efficiency, spectral resolution, and temporal window, compensation/cancellation of chirp, and generation of multiple output waveforms.**

***Index Terms*—Pulse shaping, ultrafast optics.**

I. Introduction

PULSE-SHAPING methods allowing synthesis of complex femtosecond optical waveforms according to specification are now well established [1]–[7]. As usually practiced, the output waveform is determined by the Fourier transform of a spatial pattern transferred by a mask or a modulator array onto the dispersed optical spectrum. Such Fourier transform femtosecond pulse shaping is used in many scientific applications of femtosecond optics, e.g., [8], [9], and applications in communications are also being explored [10]–[13]. However, for some communications applications, one would prefer a direct (rather than a Fourier transform) mapping between a spatial pattern and the resultant ultrafast optical waveform. One example is in parallel-to-serial conversion, where one might envision converting a parallel electronic data word to an ultrafast optical serial data packet by using a suitable pulse-shaping geometry containing an optoelectronic modulator array driven by the data word. For this purpose, it would be desirable that each bit in the output optical data packet be associated with a single modulator element, both for simplicity and because the need to compute a Fourier transform before setting the state of the modulator array would restrict operation to relatively low packet rates.

Such a pulse-shaping geometry, which we call the direct space-to-time (DST) pulse shaper, was previously demonstrated for relatively simple pulse shapes with pulse durations in the several picosecond range [14]–[17]. In recent work, we demonstrated the first operation of a DST pulse shaper for generation of femtosecond data packets [18] and developed a means for controlling the chirp in the DST pulse shaper [19], which would be important for subsequent transmission over optical fibers.

Manuscript received August 24, 2000; revised November 27, 2000. This work was supported by the Army Research Office under Contract DAAG55-98-1-0514 and by sponsors of the Center for Education and Research in Information Assurance and Security.

The authors are with the School of Electrical and Computer Engineering and Center for Education and Research in Information Assurance and Security—CERIAS, Purdue University, West Lafayette, IN 47907-1285 USA.

Publisher Item Identifier S 0018-9197(01)02326-0.

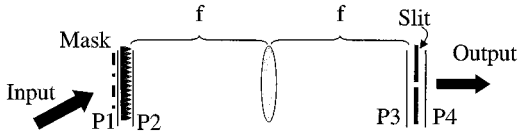

Fig. 1. Schematic representation of the pulse shaping optics in the DST shaper.

In this paper, we give a comprehensive discussion of the DST pulse shaper on a femtosecond time scale and present a number of new results, including a method for simultaneous generation of multiple wavelength-shifted, but otherwise identical, pulse sequences from the DST pulse shaper and a generalization of our previous chirp control results. Furthermore, we show how the operation of the DST pulse shaper may be understood as the femtosecond response of a generalized spectrometer.

The remainder of this paper is structured as follows. Section II contains an analysis of the DST pulse shaper under a relatively simple set of conditions and describes how the basic DST conversion function may be understood by analogy with a simple spectrometer. Section III discusses the experimental apparatus and presents results demonstrating DST conversion for both simple and highly structured optical waveforms. Tradeoffs between spectral resolution, temporal window, and efficiency are also analyzed in this section. The first complete analysis of the chirp compensation properties of the DST shaper, including experimental confirmation of this analysis, is presented in Section IV. These results show that the chirp behavior of the DST shaper is rather different from the well-known chirp behavior of Fourier transform pulse shapers or pulse stretchers [20]. Section V further extends the analysis to demonstrate the potential for simultaneously generating multiple spatially shifted output waveforms with the same output intensity profile, but different center wavelengths. This possibility, which is not available for the Fourier transform pulse shaper, is again verified by experiment. In Section VI, we conclude. This body of work represents the first comprehensive overview of the characteristics of the DST pulse shaper from both a theoretical, as well as an experimental, view.

II. DST Pulse-Shaping Description

A schematic representation of the pulse-shaping components making up the DST pulse shaper is shown in Fig. 1. A spatially patterned mask is present at the surface of a diffraction grating. A lens collects and focuses the spatially dispersed frequency components of the input beam that are diffracted from the grating. At the Fourier plane of the pulse shaping lens, a thin slit filters the dispersed spectrum, and, in the ideal case, generates a spatially homogeneous output beam whose temporal intensity profile is given by a scaled replica of the spatial masking

function present at the diffraction grating. The scaling parameter between the spatially patterned mask and the output temporal profile will be investigated in this section.

A. Quantitative Argument

The Fourier transform relations used in all the following discussions are listed for completeness:

$$\begin{aligned} F(\omega) &= \frac{1}{\sqrt{2\pi}} \int dt\, f(t)\, \exp[-j\omega t] \\ f(t) &= \frac{1}{\sqrt{2\pi}} \int d\omega\, F(\omega)\, \exp[j\omega t] \\ S(k) &= \frac{1}{\sqrt{2\pi}} \int dx\, s(x)\, \exp[jkx] \\ s(x) &= \frac{1}{\sqrt{2\pi}} \int dk\, S(k)\, \exp[-jkx]. \end{aligned} \tag{1}$$

The key planes to be investigated in the following are shown in Fig. 1. The planes P1 and P2 are located just after transmission through a spatially patterned mask and diffraction off the grating, respectively. The planes P3 and P4 are located just prior to, and just after, the output slit, respectively. If the input to the apparatus is an optical pulse of short duration with a spatial profile given by $s(x)$, then the field just before the diffraction grating is given by

$$e_1(x, t) = s(x) e_{\text{in}}(t) \propto s(x) \int d\omega\, E_{\text{in}}(\omega)\, \exp(j\omega t). \tag{2}$$

Here, $s(x)$ includes both the spatial profile of the input beam and the effect of transmission through the spatially patterned mask, $e_{\text{in}}(t)$ is the temporal profile of the input field, its Fourier transform $E_{\text{in}}(\omega)$ is the input spectrum, and x is the transverse spatial coordinate. Assuming a diffraction-grating dispersion that is linear in space and frequency yields the spectrum just after the diffraction grating [21], [22]

$$E_2(x, \omega) \propto s(\beta x)\, \exp(-j\gamma\omega x) E_{\text{in}}(\omega)$$

with the corresponding time-domain field given by

$$e_2(x, t) \propto \int d\omega\, E_2(x, \omega)\, \exp(j\omega t). \tag{3}$$

The spatial dispersion is written

$$\gamma = \frac{\lambda}{cd \cos\theta_d} \tag{4}$$

where

- λ center wavelength;
- c speed of light;
- d the period of the diffraction grating;
- θ_d angle of diffraction.

The astigmatism of the diffracting grating is included with the term

$$\beta = \frac{\cos\theta_i}{\cos\theta_d} \tag{5}$$

with the incident angle given by θ_i. If the grating-lens and lens-output slit separations are set equal to the focal length of the lens f, then the field just before the output slit is the spatial Fourier transform of (3) [23] with the result

$$e_3(x, t) \propto \int d\omega\, E_{\text{in}}(\omega) S\left(\frac{2\pi x}{\beta\lambda f} - \frac{\gamma\omega}{\beta}\right) \exp(j\omega t). \tag{6}$$

Assuming an ideal thin slit at the apparatus output, and calling the transverse output slit position $x = 0$ for convenience, yields the field just after the output slit

$$e_4(x, t) \propto \int d\omega\, E_{\text{in}}(\omega) S\left(-\frac{\gamma\omega}{\beta}\right) \exp(j\omega t). \tag{7}$$

As (7) shows, the output temporal profile is determined by the Fourier transform of the output spectrum with the result

$$e_4(t) \propto e_{\text{in}}(t) * s\left(\frac{-\beta}{\gamma} t\right). \tag{8}$$

In words, then, the output temporal profile is determined by the input field convolved with a scaled representation of the input spatial profile. The space-to-time conversion constant is given by

$$\frac{\gamma}{\beta} = \frac{\lambda}{cd \cos\theta_i}. \tag{9}$$

The spatial profile just before the surface of the diffraction grating is the product of the masking function with the input beam profile. For a Gaussian beam, we can write

$$s(x) = m(x)\, \exp\left[\frac{-x^2}{w^2}\right] \exp\left[\frac{-jk}{2R} x^2\right]. \tag{10}$$

The first term $m(x)$ represents the masking function just prior to the surface of the diffraction grating. The second term is the Gaussian spatial profile of the input beam, and the final term is a quadratic phase dependence which arises when the beam is not perfectly collimated at the grating. When (10) applies, the output temporal profile is rewritten

$$e_{\text{out}}(t) \simeq e_{\text{in}}(t) * \left\{ m\left(\frac{-\beta t}{\gamma}\right) \exp\left[\frac{-\beta^2 t^2}{\gamma^2 w^2}\right] \exp\left[\frac{-jk\beta^2 t^2}{2R\gamma^2}\right] \right\} \tag{11}$$

where $e_{\text{out}}(t)$ has replaced $e_4(t)$ as used in the above discussion in order to emphasise that this is the final temporal output field. The term inside the $\{\cdots\}$ is the impulse response function of the DST shaper. It consists of a scaled version of the mask, multiplied by a Gaussian temporal window function corresponding to the input Gaussian beam profile, as well a quadratic temporal phase variation which arises when the phase fronts at the grating are not planar. In the remainder of this section, we concentrate on the intensity behavior of the shaped output. In Section IV, we discuss the chirp corresponding to the quadratic temporal variation, as well as its compensation.

B. Qualitative Argument

Alternative descriptions of the basic operation of the DST shaper can be obtained by exploring the fundamental pulse-shaping components and configuration shown in Fig. 1. First, the space-to-time conversion constant can equally be determined by examining the pulse-tilt for a collimated plane

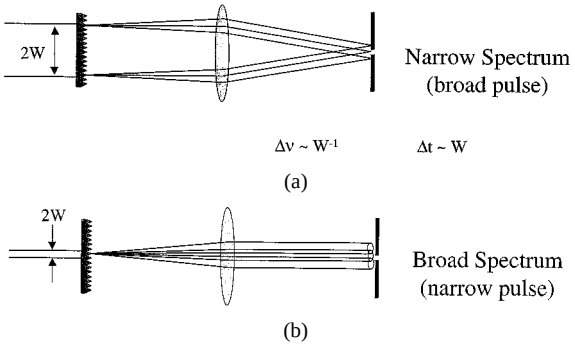

Fig. 2. Spectrometer analogy for the space-time scaling of the DST shaper.

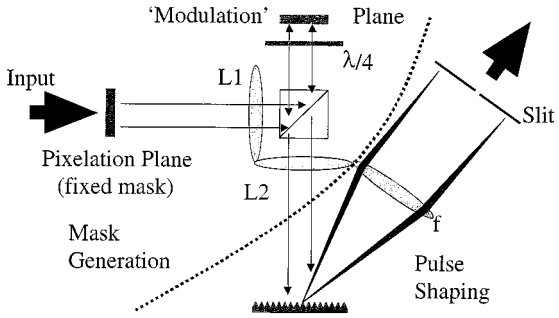

Fig. 3. Complete DST apparatus.

wave diffracted off of a grating [24]. The pulse-tilt, or delay across the diffracted beam relative to the input beam size derived from [24] or a simple trigonometric argument, exactly gives the space-to-time conversion constant (9).

Second, the configuration shown in Fig. 1 will be recognized as a spectrometer arrangement with the addition of a spatially patterned mask on top of the diffraction grating. If a spectrometer (without a spatially patterned mask) is configured for maximum spectral resolution (large beam on the diffraction grating, and thin output slit), the output obviously consists of a narrow spectral feature. If the input consists of a short temporal-duration optical pulse, then the output pulse, in time, is broadened with respect to the input due to the spectral filtering performed by the spectrometer, as shown in Fig. 2(a). If the apparatus configuration is unperturbed, except that the size of the input beam is decreased, as shown in Fig. 2(b), the resolution of the spectrometer is decreased as well. If one considers the input to be a short optical pulse again, then the output spectrum is broadened with respect to the previous case, or the temporal duration of the output is decreased with respect to the previous case. The width of a mask, which simply modifies the spatial extent of the beam on the diffraction grating, can then be seen to modify the temporal duration of the apparatus output directly. This argument illustrates the operation of the DST pulse shaper in a very simple case and shows its relation to a classical optical spectrometer. In the course of this paper, we will extend these results to understand the femtosecond response of a generalized spectrometer, allowing generation of complex optical waveforms, control and compensation of chirp, and the possibility of obtaining multiple wavelength-shifted versions of a femtosecond pulse sequence simultaneously.

III. DST Apparatus

A. Complete Apparatus

The schematic representation of the DST pulse shaper shown in Fig. 1 is convenient for understanding the space- time mapping of the apparatus. However, in practice, a slightly more complex apparatus provides substantial additional flexibility. The complete DST pulse shaping apparatus is shown in Fig. 3. The pulse-shaping components discussed in the previous section are present to the right of the dashed line, while the mask generation optics are to the left of the dashed line. For the experiments to be discussed in the following, a Ti : sapphire laser producing 100-fs pulses at a center wavelength of 850 nm is used as the input to the DST pulse shaper.

The output beam from the source laser is spatially patterned by transmission through a fixed amplitude mask consisting of a 1-D array of transparent rectangles in an otherwise opaque background. The spatially patterned beam at the "pixelation plane" is imaged by the lens L1, a 100-mm focal length condensor lens, onto the "modulation plane" through a polarizing beamsplitter cube and quarter-wave plate. The size (20 μm square) and pitch (62.5 μm center-to-center) of the transparent elements in the fixed mask, as well as the imaging condition of the first lens, have been selected to provide direct compatibility with a high-speed optoelectronic reflection modulator array. This feature is included so that, in future experiments, individual spatial locations may be set to either a high reflectivity state or a low state in a programmable fashion. For the work described here, the "modulation plane" consists of a simple mirror. The spatially patterned beam reflected from the "modulation plane" is imaged, back through the quarter-wave plate/polarizer combination, onto the diffraction grating (1800 lines/mm) by the lens L2, a 75-mm focal length condensor lens. The pulse-shaping lens is a 160-mm focal length achromat. The function of all the mask generation optics is to transfer a 1-D spatially patterned intensity profile from the apparatus input to the diffraction grating. The space-to-time conversion constant, γ/β is referenced to the surface at, but before diffracting off, the grating. In order to relate γ/β to the apparatus input, (9) must be multiplied by *mag*, the overall imaging system magnification of the mask generation optics. The imaging system magnification is determined by the placement of the spatially patterned mask, "modulation plane," and diffraction grating, as well as the focal lengths of the two imaging lenses. In practice, the first imaging operation (from the pixelation mask to the "modulation plane") is set for unity magnification, while the second imagining operation (from the "modulation plane" to the grating) is set for a magnification in the range of 4–6.5.

B. Measuring the Space-to-Time Conversion Constant

A simple measurement of the space-to-time conversion constant, and a first example of pulse shaping with the DST, is shown in Fig. 4. A thin slit replaces the spatially patterned mask at the "pixelation plane," and intensity cross-correlations are recorded of the output pulses using a reference pulse directly from the source laser for several different transverse positions of the slit at the pixelation plane. The delay shift between traces

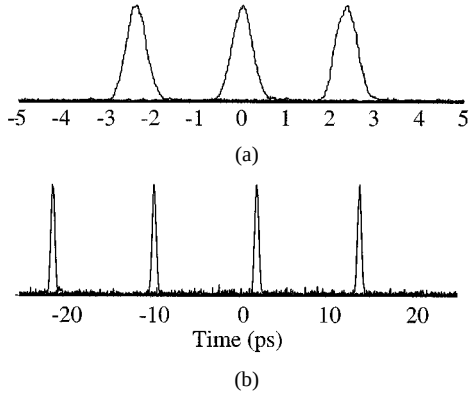

Fig. 4. Measurement of the space-to-time conversion constant for imaging system magnifications of: (a) 4.2 and (b) 6.5.

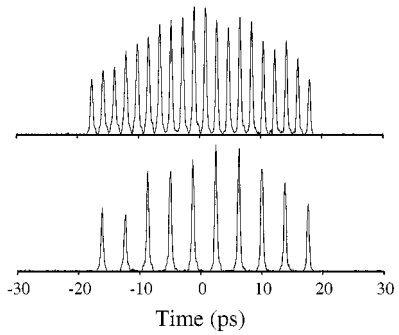

Fig. 5. Pulse train generation using a periodic pixelation mask.

gives a measurement of the space-to-time conversion constant including *the imaging system magnification.* In the top series of Fig. 4, a 25-μm slit is moved ± 80 μm from the center of the input beam with an imaging system magnification of 4.2. Measuring the change in delay from one trace to the next gives a measured space-to-time conversion constant of 29.6 ps/mm. Using the measured diffraction angle of the grating (54°), the expected space-to-time conversion constant is calculated to be 30.7 ps/mm. A second example of measuring the space-to-time conversion constant is given in Fig. 4(b). In this case, a 20-μm slit is translated in 250-μm increments across the pixelation plane with an imaging system magnification of 6.5. The measured space-to-time conversion constant is 47.0 ps/mm, in excellent agreement with the calculated value of 47.5 ps/mm. In both the cases shown in Fig. 4, the space-to-time conversion constant for the pulse shaping components, given by (9), is held fixed, thus demonstrating the space-time scaling change possible with the geometry of the imaging system.

C. Pulse-Train Generation

One target application of the DST pulse shaper is in the generation of trains of pulses, or pulse sequences, where the state of each pulse in the train, either "ON" or "OFF," is set by the optical transmission at a specific spatial location. In order to demonstrate the pulse-train generation capabilities of the DST pulse shaper, a periodic fixed mask is inserted at the pixelation plane. Fig. 5 shows the output pulse shapes, recorded by intensity cross-correlation for two different periodic pixelation patterns and an imaging system magnification of 4.2. The top trace

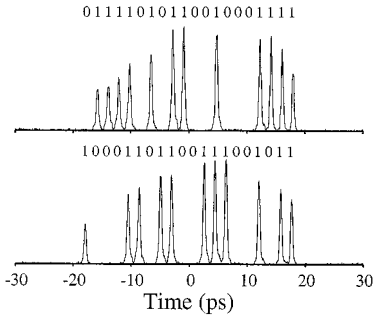

Fig. 6. Optical "data packet" generation from the DST shaper.

corresponds to a mask with 20 transparent rectangles 20-μm wide with 62.5-μm center-to-center spacing. This mask generates a train of 20 pulses. The pulse period, 1.88 ps, is in excellent agreement with the value expected from the space-to-time conversion constant, 7.3 ps/mm, and imaging system magnification. The bottom trace shows a similar case where every other transparent feature of the pixelation mask is blocked. As expected, a train of ten pulses with twice the period of the previous case is measured at the apparatus output. In both of these cases, the output pulse train is observed to be superimposed on a roughly Gaussian window. The rolloff in the temporal profile is due to the input beam profile at the pixelation mask, and the extent of the temporal window is determined from the input beam profile and the effect of the finite-width pulse-shaping slit, as will be discussed in the following section. If a uniform pulse train is desired, a diffractive optical element (DOE) could be used instead of the pixelation mask as a "spot-generator" [25].

Fig. 6 shows two final examples of pulse sequence generation with the DST apparatus. In these cases, individual spatial locations within the 20-element pixelation mask are blocked. The resulting DST output, again recorded via intensity cross-correlation with a short reference pulse directly from the source laser, is a "pulse packet." These data demonstrate the parallel-to-serial conversion property of the DST pulse shaper that may play an important role in optical communications. All of the data shown here have been generated using a fixed pixelation mask to control the spatial pattern present at the diffraction grating. Equivalently, an optoelectronic modulator array could be used at the "modulation plane" shown in Fig. 3 to electronically control the transmission of each spatial location. Of course, the excellent ON–OFF contrast apparent in Figs. 5 and 6 would then be limited by the actual contrast provided by the modulator array.

D. Spectral Resolution, Temporal Window, and Efficiency of the DST Pulse Shaper

So far, we have assumed a very thin (delta function) slit at the output of the DST apparatus. Although this provides an ideal pulse shaping response, it is not practical, since the transmitted power would be zero. In the following we analyze the trade-off between optical efficiency, spectral resolution, and the pulse shaping temporal window which occurs with a pulse shaping slit of finite width.

First, recall that the field just prior to the output slit is determined by the input spectrum multiplied by the spatial Fourier transform of the *spatial* profile at the diffraction grating in (6).

We now introduce a general slit with amplitude transmittance $a(x/x_o)$, where x_o allows the width of the output slit to be scaled. The field after the slit is now given by

$$e_4(x,t) \propto \int d\omega\, a\left(\frac{x}{x_o}\right) E_{\text{in}}(\omega) S\left(\frac{2\pi x}{\beta\lambda f} - \frac{\gamma\omega}{\beta}\right) \exp(j\omega t). \tag{12}$$

Unlike the case of a delta-function slit, the field is now a nonseparable function of space and time; the actual field seen by an experiment depends on where the experiment is placed and any spatial filtering between the DST output slit and the experiment. In many cases, it will be the on-axis field after diffraction into the far field that will be of interest. This situation is easily treated analytically, since the diffraction into the far-field is equivalent to a spatial Fourier transform, which should be evaluated at $x = 0$ to obtain the on-axis field. The result for the far-field on-axis output can be shown to be

$$e_{\text{out}}(t) \propto e_{\text{in}}(t) * \left[\left(\frac{-\beta}{\gamma}\, t\right) A\left(\frac{2\pi x_o t}{\lambda\gamma f}\right)\right] \tag{13}$$

where $A(k)$ is the Fourier transform of the slit function. Similarly, the output spectral amplitude is given by

$$E_{\text{out}}(\omega) \propto E_{\text{in}}(\omega)\left[S\left(\frac{-\gamma\omega}{\beta}\right) * a\left(\frac{\lambda\gamma f\omega}{2\pi x_o}\right)\right]. \tag{14}$$

The terms inside the $[\cdots]$ signs of (13) and (14) give the impulse response function and spectral filter function of the DST pulse shaper, respectively. For a sufficiently short input pulse, these give the pulse shape and the spectral amplitude of the output pulse. In the case of a perfectly collimated input beam ($R = \infty$), we can rewrite the output field in terms of the masking function and the input Gaussian beam profile, which gives the following:

$$e_{\text{out}}(t) \propto e_{\text{in}}(t) * \left[m\left(\frac{-\beta}{\gamma}\, t\right) \exp\left(\frac{-\beta^2 t^2}{\gamma^2 w^2}\right) A\left(\frac{2\pi x_o t}{\lambda\gamma f}\right)\right] \tag{15}$$

and

$$E_{\text{out}}(\omega) \propto E_{\text{in}}(\omega)\left[M\left(\frac{-\gamma\omega}{\beta}\right) * \left\{\exp\left(\frac{-\gamma^2 w^2\omega^2}{4\beta^2}\right) * a\left(\frac{\lambda\gamma f\omega}{2\pi x_o}\right)\right\}\right]. \tag{16}$$

These equations lead to several important observations.

1) The impulse response function of a generalized spectrometer (i.e., the DST pulse shaper) is the inverse Fourier transform of the spectral filter function even for an arbitrary input spatial profile.
2) The spectral filter function is given by the convolution of appropriately scaled versions of the slit function and the Fourier transform of the input spatial profile, even for arbitrary input spatial profiles and slit functions. A similar convolution governs the spectral resolution of an ordinary spectrometer, where simple input spatial profiles and slit functions are usually considered. In general, the width of the filter function increases (spectral resolution degrades) as the width of the slit function (x_o) increases.
3) The impulse response function is given by the product of appropriately scaled versions of the spatial profile and the Fourier trpansform of the slit function. Thus, the finite width of the slit leads to a temporal window function which restricts the temporal range of output waveforms generated by the DST pulse shaper. The width of the temporal window is inversely proportional to the width of the slit. For a rectangular slit. where $a(u) = 1$ for $|u| < 1/2$ and zero otherwise, the temporal window function is a sinc with an intensity FWHM

$$T_{\text{slit}} = \frac{0.886\gamma\lambda f}{x_o}. \tag{17}$$

In the case of a Gaussian input beam before the mask, the output may also be written as the product of the scaled masking function times a window function consisting of a Gaussian rolloff term times the scaled Fourier transform of the slit function.
4) The effect of the finite slit-width is the same as multiplying the input spatial profile by a spatial windowing function given by $A(-2\pi x_o x/\lambda\beta f)$, while at the same time setting the width of the slit to zero.

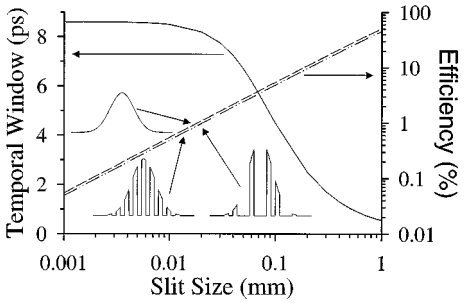

Fig. 7. Temporal window (solid) and efficiency (dash and dot-dash) as a function of pulse-shaping slit width. The inset shows the spatial field profile present at the diffraction grating for the efficiency calculations. The dashed line is for a Gaussian profile, while the result for both patterned spatial profiles is indicated by the dashed-dotted line.

Fig. 7 shows the calculated temporal window (in terms of the FWHM of the intensity) as a function of pulse-shaping slit width. The space-to-time conversion constant was set to 7.3 ps/mm, with unity imaging system magnification, and the input beam shape was a simple Gaussian beam with radius w=1.0 mm just before the grating. For slit widths below approximately 30 μm, the temporal window is limited only by the Gaussian beam size and is nearly independent of slit width. Thus, in this calculation, the approximation of a delta-function output slit is valid for slit widths up to $\sim$30μm. Significantly above this value, the temporal window decreases roughly inversely with the slit width.

A simple measure of efficiency can be calculated by integrating the power coming through the slit relative to the total power before the slit

$$\eta = \frac{\iint dx\, d\omega \left| S\left(\frac{2\pi x}{\beta\lambda f} - \frac{\gamma\omega}{\beta}\right) E_{\text{in}}(\omega) a\left(\frac{x}{x_o}\right)\right|^2}{\iint dx\, d\omega \left| S\left(\frac{2\pi x}{\beta\lambda f} - \frac{\gamma\omega}{\beta}\right) E_{\text{in}}(\omega)\right|^2}. \quad (18)$$

This expression does not take into account any spatial selection of the diffracted output field by the experiment, but is useful as an upper limit to the available output power. The calculated result for the efficiency is also shown in Fig. 7, assuming a 300-fs duration (FWHM) transform-limited Gaussian input pulse and three different input spatial profiles. We first discuss the case of no pixelation mask, i.e., a simple Gaussian spatial input profile as above (dashed line). The efficiency increases linearly as the slit width increases. Note that when a transform limited input pulse of duration t_p is spectrally sliced to generate a longer bandwidth-limited pulse of duration T, the best-case efficiency scales as t_p/T times a numerical factor of order unity. The DST pulse shaper achieves this best case for wide slit-widths when the temporal window is determined mainly by the slit width. In this limit, T is proportional to the inverse of the slit width and, therefore, the efficiency is proportional to the inverse of T. When the slit width is decreased below the regime where the spectral resolution and temporal window are limited by the slit, further reduction of the slit width reduces the efficiency without improving spectral resolution or temporal window. In this case, the best-case efficiency is not achieved. Therefore, for optimum efficiency the slit width should be adjusted to the largest width consistent with the required temporal window.

Fig. 7 also shows the result of efficiency calculations for two other spatial input patterns. One case is a periodic spatial masking function consisting of 250-μm wide clear apertures with a 500-μm period. The other case is an example of a pulse packet where some of the clear apertures in the periodic masking function are made opaque. The inset of Fig. 7 shows the input spatial field profile used in the calculation in each of the three cases, including the unmasked Gaussian beam. The efficiencies are essentially indistinguishable for the two masked cases (dashed-dotted lines), which are also very close but slightly below the efficiency in the unmasked case. The integrated intensity in the input masked spatial profile is held constant in each case, as would be the case if a DOE is used to spatially pattern the input beam without loss. If loss is incurred in shaping the input spatial profile, e.g., by using an amplitude mask, this reduces the overall system efficiency to a level below that predicted by (18). Notice that, for a fixed input pulse and temporal window, the efficiency is roughly independent of the masking function. This behavior was previously predicted in [18].

We can gain further insight into these trends when the following two conditions hold.

1) The slit function $a(x/x_o)$ is much narrower then the finest features in $S(2\pi x/\beta\lambda f)$. This is the narrow slit limit, in which the temporal window is limited by the input beam size rather then by the slit. This is the most interesting regime for the DST pulse shaper.
2) $S(-\gamma\omega/\beta)$ is much narrower than $E_{\text{in}}(\omega)$. This means that the input pulse is much narrower then the narrowest temporal features in the scaled spatial profile $s(-\beta t/\gamma)$.

With these assumptions, for the efficiency (18) simplifies to

$$\eta \approx \frac{\frac{2\pi}{\gamma\lambda f}\int dx \left| a\left(\frac{x}{x_o}\right)\right|^2}{\int d\omega \left|\frac{E_{\text{in}}(\omega)}{E_{\text{in}}(0)}\right|^2}. \quad (19)$$

In this limit, which corresponds to slit widths below $\sim$30 μm in Fig. 7, the efficiency is independent of the masking function. This expression can be further simplified if, for example, we assume a rectangular slit of width x_o and a Gaussian input pulse of the form $e_{\text{in}}(t) \sim \exp(-t^2/t_p^2)$. The efficiency becomes

$$\eta \approx \frac{\sqrt{2\pi}\, x_o t_p}{\gamma\lambda f}. \quad (20)$$

The efficiency increases linearly with slit width, provided that assumption (1) remains valid. The best efficiency possible for a given temporal window T can be estimated by increasing x_o until the temporal window due to the slit decreases to T. Using (17) to replace x_o in terms of T, one obtains

$$\eta \approx 2.2\,\frac{t_p}{T}. \quad (21)$$

This expression should be taken as approximate, since assumption (1) is beginning to be violated. Nevertheless, this result is consistent with our discussion above and indicates that the best-case efficiency scales as the ratio of the input pulse width to the temporal window, independent of the detailed shape of the output waveform. Equations (19)–(21) explain all the key features of the efficiency curves observed in the numerical results for the narrow-slit regime ($x_o < \sim$30 μm). It is interesting to note that the same behavior continues to hold in the cases examined, even in the wide-slit regime ($x_o > \sim$30 μm) for which the assumptions made above do not hold.

Finally, we note that instead of considering a slit function as above, it is also possible to replace the output slit with a waveguide. This case is relevant to integrated spectrometer devices such as arrayed waveguide grating demultiplexors [26] used in WDM communications. When the output slit is replaced by a single-mode waveguide, a spatially uniform output field is produced automatically with no further spatial filtering. The temporal window and efficiency can be computed exactly by calculating the overlap integral of the field with the waveguide on a frequency by frequency basis. Although the details are not given here, we note that important features discussed above, such as the Fourier transform relationship between the spectral filter function and the temporal impulse response function, remain valid. A complete description of the analogy between the bulk optics DST pulse shaper and the integrated-optics arrayed waveguide grating, used for the generation of very-high repetition rate pulse bursts, is contained in [].

IV. Chirp in the DST Apparatus

A. Effect of Input Phase Curvature

The imaging operations shown in Fig. 3 have one side effect that has thus far not been discussed: in addition to relaying the desired intensity profile of the pixelated input beam onto the diffraction grating, the imaging operation places a quadratic spatial phase variation on the grating as well. The space-to-time conversion property of the DST operates on this spatial phase variation as well as on the intensity profile. The quadratic spatial phase is transformed into a quadratic temporal phase on the output waveform, and, hence, a chirp.

The magnitude and sign of the chirp attributable to the apparatus itself can be calculated if we assume a very short input pulse and assume $m(x) = 1$, i.e., there is no pixelation mask. Then (11) can be simplified to

$$e_{\text{out}}(t) \simeq \exp\left[\frac{-\beta^2 t^2}{\gamma^2 w^2}\right] \exp\left[\frac{-jk\beta^2 t^2}{2R\gamma^2}\right]. \tag{22}$$

This is of the form

$$e(t) \propto \exp[-\Gamma t^2] \tag{23}$$

where the carrier term $\exp(j\omega_o t)$ is implied, and Γ has both real and imaginary parts

$$\Gamma = \Gamma_r + j\Gamma_i \tag{24}$$

with $\Gamma_r = \beta^2/\gamma^2 w^2$ and $\Gamma_i = k\beta^2/2R\gamma^2$. The instantaneous frequency is given by the time derivative of the total phase

$$\omega_{\text{inst}}(t) = \frac{\partial \phi_{\text{total}}}{\partial t} = \frac{\partial}{\partial t}(\omega_o t - \Gamma_i t^2) \tag{25}$$

and the chirp, sometimes called a frequency modulation, is given by the time derivative of the instantaneous frequency

$$\frac{\partial \omega_{\text{inst}}}{\partial t} = -2\Gamma_i. \tag{26}$$

Finally, it is convenient to express the chirp in terms of wavelength instead of frequency with the result

$$\frac{\partial \lambda}{\partial t} = \frac{\Gamma_i \lambda^2}{\pi c} = \frac{\lambda \beta^2}{cR\gamma^2}. \tag{27}$$

Expressed in terms of the fundamental parameters of the DST pulse shaper, the chirp is given by

$$\frac{\partial \lambda}{\partial t} = \frac{cd^2 \cos^2 \theta_i}{R\lambda}. \tag{28}$$

With this result, it is possible to estimate the chirp expected to be present on the output of the DST pulse shaper.

B. Chirp Measurement

In order to measure the chirp on the output of the DST pulse shaper, the pixelation mask is replaced by a single slit. As in Fig. 4, a single output pulse is generated from the DST shaper with this pixelation mask. The width of the pixelation mask is chosen as a tradeoff between the output pulse width and the width of the power spectrum at the apparatus output. Fig. 8 shows results of our chirp measurement. The pixelation mask is translated across the input beam, and intensity cross-correlations and power spectra are recorded as a function of pixelation mask position. The center wavelengths of the measured power spectra are plotted as a function of the time delays corresponding to each of the transverse pixelation mask positions. The slopes of the two curves in Fig. 8 are measures of the DST chirps for different imaging system magnifications. The slopes are 6.4 and 6.8 ps/nm for imaging system magnifications of 4.2 and 6.5, respectively.

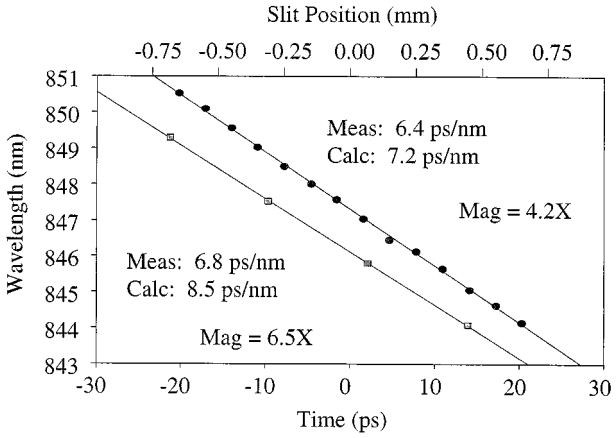

Fig. 8. Measurement of apparatus chirp for two imaging system magnifications.

A theoretical estimate of the expected chirp on the DST output can be obtained by numerically propagating a beam through the imaging system optics using Gaussian beam methods (ABCD matrices) [28], [29] in order to determine an expected phase-front curvature at the surface of the diffraction grating. Assuming a flat phase front at the surface of the pixelation mask, estimated values of chirp are 7.2 and 8.5 ps/nm for imaging system magnifications of 4.2 and 6.5, respectively, which are in reasonable agreement with the experimental values. The difference between the measured and calculated chirps is due to the fact that the phase front is not completely flat at the pixelation mask.

C. Diffraction Analysis: Chirp Compensation by the DST Apparatus

If the DST apparatus is to be used in optical communications applications, it will usually be necessary to control the chirp, and possibly set it to zero. One way to eliminate the chirp in the DST apparatus would be to utilize a telescopic configuration for relaying the masked spatial profile from the apparatus input to the diffraction grating. However, a flat phase front would be present at the diffraction grating only if a perfectly collimated (or focused) beam were present at the apparatus input with a precisely positioned telescopic configuration. Since these strict requirements may be undesirable in some cases, it is useful to explore alternative methods for eliminating the final term of (22).

To this end, we have performed a diffraction analysis of the DST apparatus [19]. Similar analyses have been previously performed for pulse stretchers [21] and pulse shapers [22]. In [19], we showed that changing the pulse shaping lens-output slit separation introduces a quadratic temporal phase term (chirp) to the output field that can be used to cancel the chirp resulting from the phase front curvature present at the diffraction grating. In the following, we generalize the diffraction analysis in order to permit both the grating-lens and lens-slit separations to vary.

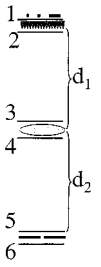

Fig. 9. Diffraction analysis planes of interest.

Fig. 9 shows a schematic representation of the different propagation regions included in the diffraction analysis. The grating-lens and lens-slit separations are denoted d_1 and d_2, respectively. Following a procedure similar to [21] and [22], and starting with (3), the spectral amplitude of the field just prior to the diffraction grating is written

$$E_2(x,\omega) \propto s(\beta x)\,\exp[-j\gamma\omega x]E_{\text{in}}(\omega). \tag{29}$$

The field just after the grating is propagated in the Fresnel regime to just before the pulse shaping lens [23], giving the following new expression for the spectral amplitude:

$$E_3(x,\omega) \propto \int_{-\infty}^{\infty} dx_2 E_2(x_2,\omega)\,\exp\left[\frac{jk}{2d_1}x_2^2\right] \cdot \exp\left[\frac{-jk}{d_1}x_2 x\right]. \tag{30}$$

Then the effect of the lens is included

$$E_4(x,\omega) = E_3(x,\omega)\,\exp\left[\frac{-jk}{2f}x^2\right] \tag{31}$$

followed by another propagation in the Fresnel regime to the output slit

$$E_5(x,\omega) \propto \int_{-\infty}^{\infty} dx_4 E_4(x_4,\omega)\,\exp\left[\frac{jk}{2d_2}x_4^2\right] \cdot \exp\left[\frac{-jk}{d_2}x_4 x\right]. \tag{32}$$

Finally, the effect of a delta-function output slit is included:

$$E_6(x,\omega) = E_5(x,\omega)\delta(x). \tag{33}$$

In order to relate the input and output fields, (29)–(33) are combined with (10) for $s(x)$ and the identity [30]

$$\int_{-\infty}^{\infty} dx\,\exp[j(\alpha x^2+\xi x)] = \sqrt{\frac{j\pi}{\alpha}}\,\exp\left[\frac{-j\xi^2}{4\alpha}\right]. \tag{34}$$

After considerable manipulation, we obtain the result

$$e_{\text{out}}(t) \propto e_{\text{in}}(t) * \{N(t)\,\exp[-j\phi(t)]\} \tag{35}$$

where

$$N(t) = m\left(\frac{-\beta t}{\gamma}\right)\exp\left[\frac{-\beta^2 t^2}{\gamma^2 w^2}\right] \tag{36}$$

determines the temporal intensity profile of the output, and

$$\phi(t) = \frac{k}{2\gamma^2}\left(\frac{\beta^2}{R} - \frac{d_2 - f}{d_1 f + d_2 f - d_1 d_2}\right)t^2 \tag{37}$$

gives the quadratic temporal phase and, hence, the chirp. The output chirp can be manipulated (in a special case compensated or set to zero) by varying d_1 and d_2. The intensity profile and space-to-time conversion constant are expected to remain invariant as the chirp is manipulated in this way.

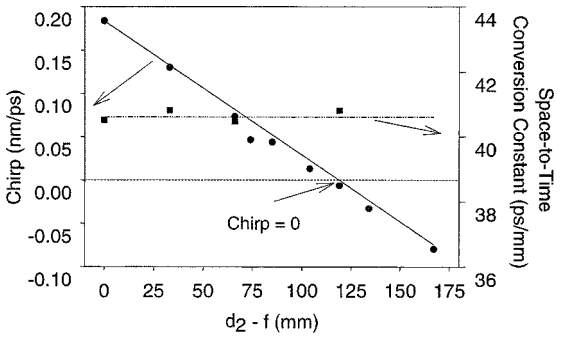

Fig. 10. Chirp and space-to-time conversion constant measured as the pulse shaping lens-slit separation is varied.

Unlike the well-known grating and lens pulse stretcher [21], the chirp is most strongly affected by the lens-slit separation (d_2). When d_2 is fixed at the focal length of the lens ($d_2 = f$), output chirp is independent of the diffraction grating-lens separation, d_1. Further, for bandwidth-limited input pulses, the measured chirp in the $d_2 = f$ case can provide a measure of the phase front curvature at the surface of the diffraction grating, R. After determining the value of R in this way, the chirp can be calculated as a function of d_1 and d_2 with no further adjustable parameters using (27), with Γ_i replaced by

$$\Gamma_i = \frac{k}{2\gamma^2}\left(\frac{\beta^2}{R} - \frac{d_2 - f}{d_1 f + d_2 f - d_1 d_2}\right). \tag{38}$$

The output chirp can be set to zero by adjusting d_1 and d_2 to achieve $\Gamma_i = 0$ (again assuming unchirped input pulses). It is interesting to note that in the case of a converging or diverging input beam at the grating (i.e., $R \neq \infty$), *the beam is brought to a focus at a position* other than the back focal plane of the lens. By using ABCD matrices, one can easily show that for d_1 and d_2 yielding $\Gamma_i = 0$, an input Gaussian beam with phase front radius of curvature R is brought to focus at exactly the position of the pulse shaping slit.

D. Chirp Compensation Experimental Verification

In order to verify the predictions made in the previous section, we have performed a series of chirp measurements as outlined in Section IV-B. The predicted and measured chirp are compared, with the value of R determined from the measured chirp in the configuration $d_1 = d_2 = f$.

Fig. 10 shows the measured chirp, in nanometers per picosecond, and space-to-time conversion constant as a function of the deviation of the pulse shaping lens-slit separation d_2, away from the focal length of the pulse shaping lens. These data were recorded for the configuration where the diffraction-grating-pulse shaping lens separation was fixed at the focal length of the lens ($d_1 = f$). The predicted and measured chirp are in excellent agreement over a large range of lens-slit separations. A chirp-free output is achieved for d_2 approximately 119-mm beyond the back focal plane of the lens. Further, the space-to-time conversion constant is observed to be flat as the chirp is varied over a wide range. This provides

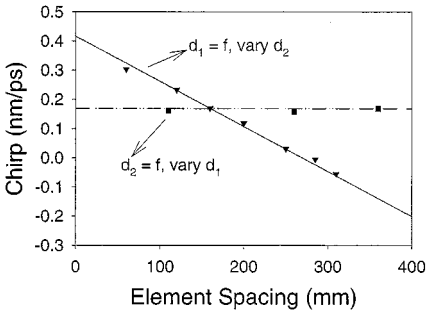

Fig. 11. Chirp in two special cases. Solid: fixed grating-pulse shaping lens separation and vary lens slit. Dashed: fixed lens-pulse shaping slit while varying grating-lens separation.

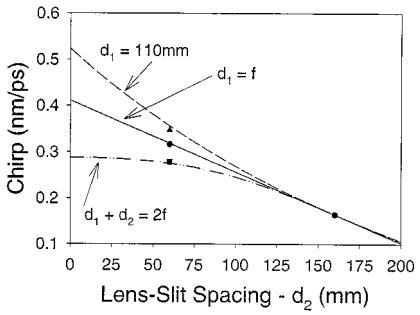

Fig. 12. Measurement of chirp in the general case.

a first indication that the output intensity profile is invariant as the chirp is varied.

Fig. 11 shows the measured chirp in two special cases. In one case, the diffraction grating-pulse shaping lens separation d_1 is allowed to vary while the pulse shaping lens-output slit separation d_2 is fixed at the focal length of the lens f. In the second case, the converse is true: d_2 is varied while $d_1 = f$ is maintained. In the first case, the output chirp does not change with d_1, as expected from our prediction. The second case is data similar to that shown in Fig. 10, and is repeated just for reference.

Two specific implementations of the general case (neither d_1 nor d_2 equal to f) are shown in Fig. 12, along with the special case of $d_1 = f$. In the top trace, the grating-lens separation is set to a fixed value of 110 mm (compared to f =160 mm), and the predicted chirp is plotted as a function of the lens-slit separation d_2. In the bottom case, both d_1 and d_2 are varied, but their sum is held fixed at twice the focal length of the lens. Both of these new cases are tested by a chirp measurement at d_2 =60 mm. In each case, the calculated and measured chirp are in excellent agreement.

Finally, in order to verify that the output intensity profile is invariant as the chirp is adjusted, intensity cross correlation traces of an ultrafast data packet were recorded for three different amounts of output chirp. The results are shown in Fig. 13, and in all cases $d_1 = f$. The top trace was taken in a moderately chirped configuration when $d_2 = f$. The middle trace was taken in a partially compensated chirp configuration, $d_2 - f$ =66 mm, and the bottom trace was taken in a chirp-free configuration, $d_2 - f$ =119 mm. The general shape of each of the three cross-correlation traces is the same, verifying that the output intensity profile is unchanged as the chirp on the DST output

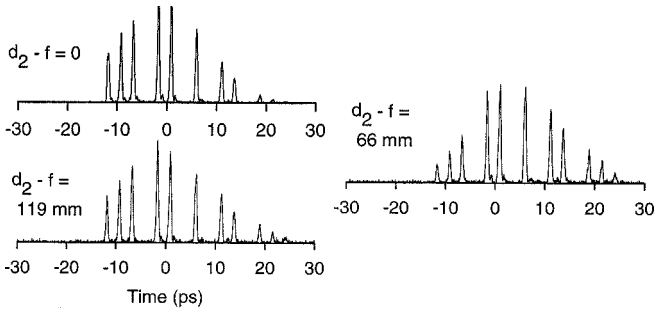

Fig. 13. Output intensity profiles measured by cross correlation with an unshaped reference pulse for pulse shaping lens-slit separations of 160, 226, and 279 mm.

is varied. The minor differences in the envelopes of the three traces is due to slight changes in the centering of the pixelation mask on the input beam from one measurement to the next.

V. Multiple Output Channels from the DST Pulse Shaper

In all the discussions thus far, a single output slit has been assumed, with the implication that this slit is centered on the dispersed frequency spectrum. Specifically, the ideal output slit was taken to be positioned at an arbitrary, but convenient position, $x = 0$. As we shall see, any other transverse position of the output slit yields exactly the same intensity profile as (8), but with a wavelength shift. In fact, a multiple element slit could be used instead of the single slit resulting in multiple spatially separated output beams. This section will focus on the output multiple wavelength nature of the DST apparatus.

A. Mathematical Description

The multiple-output nature of the DST apparatus follows directly from the previous discussions of the space–time mapping. In the following, for convenience, the DST apparatus is assumed to be configured chirp-free. That is, the pulse-shaping lens-output slit separation d_2 is set to cancel the quadratic temporal phase term due to the phase front radius of curvature at the diffraction grating. However, the important features derived below also hold for the more general case where the chirp is not compensated. In the chirp-free case, the spatial profile mapped to the time domain consists of just the first two terms of (10), the masking function, and the beam profile

$$s(x) = m(x)\,\exp\left[\frac{-x^2}{w^2}\right]. \tag{39}$$

The complex spectrum just prior to the output slit(s) is given by

$$E_3(x,\,\omega) \propto S\left(\frac{2\pi x}{\beta\lambda f} - \frac{\gamma\omega}{\beta}\right) E_{\text{in}}(\omega). \tag{40}$$

Consider now a thin slit at lateral position x_s, i.e., of the form $\delta(x - x_s)$. The filtered spectrum now has the form

$$E_4(x,\,\omega) \propto S\left(\frac{2\pi x}{\beta\lambda f} - \frac{\gamma\omega}{\beta}\right) E_{\text{in}}(\omega)\delta(x - x_s). \tag{41}$$

Note that $S(\cdots)$ is the spectral response function of the generalized spectrometer. Equation (41) shows that a transverse

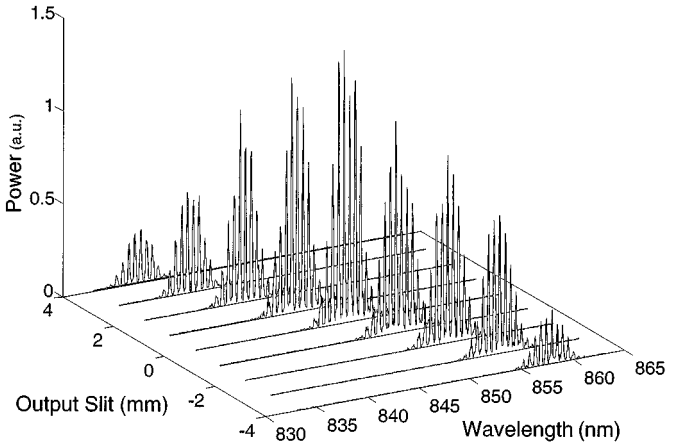

Fig. 14. Output power spectra as a function of transverse pulse-shaping slit position.

movement of the output slit leads to a simple shift in the spectral response function of the DST pulse shaper, just as it would in an ordinary spectrometer, even though the spectral response of the DST may be much more complex than that of a spectrometer.

The time domain response corresponding to (41) is given by

$$e_{\text{out}}(t) \propto e_{\text{in}}(t) * \left\{ s\left(\frac{-\beta t}{\gamma}\right) \exp\left[\frac{j2\pi x_s}{\gamma \lambda f}\, t\right] \right\}. \qquad (42)$$

The impulse response function is given by the terms inside the $\{\cdots\}$ sign and consists of two terms. The first, $s(-\beta t/\gamma)$, represents the space-to-time conversion constant and is unchanged compared to our earlier treatment. The second, linear-phase term represents a frequency shift. Thus, a lateral movement of the output slit tunes the output optical frequency while leaving the intensity profile of the shaped output waveform unaffected.

We can also consider a multiple-output slit element which spatially separates each output beam in a nonoverlapping manner. The output from each independent slit is still given by (41) and (42), with the appropriate slit position inserted for x_s. Thus, the DST pulse shaper should be able to simultaneously generate multiple spatially separated, wavelength-shifted outputs, each with the identical intensity profile. In cases where such multiple outputs are useful, this increases the overall optical efficiency by a factor equal to the number of outputs.

B. Measurements

In order to demonstrate the shift in output center wavelength as a function of transverse output slit position, a periodic pixelation mask consisting of 20 transparent rectangles in an otherwise opaque background was inserted into the pixelation plane of the DST pulse shaper. As shown previously, use of this pixelation mask will result in a temporal output intensity profile that is a train of pulses. Accordingly, one expects this output temporal profile to correspond to a periodically modulated power spectrum after the output slit. Fig. 14 shows a series of nine power spectra recorded at periodic transverse output slit positions separated by 1 mm. The trend of a shift in center wavelength as a function of transverse output slit position is quite evident when plotted in this manner. Further, Fig. 14 shows that multiple, spatially separated output channels could be generated by replacing the single-output slit used in these measurements with a multiple-element slit.

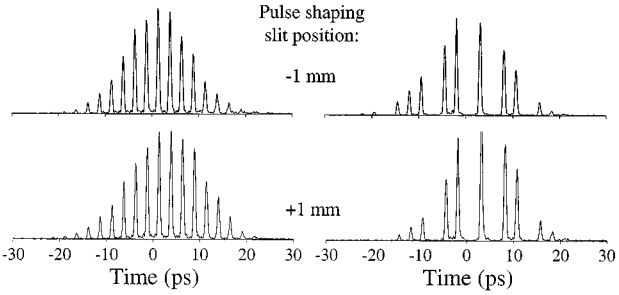

Fig. 15. Output intensity profiles for pulse-shaping slit positions separated by 2 mm and two different pixelation masks.

The invariant shape of the output power spectra in Fig. 14 implies that the temporal profile of each output is invariant as well. Further evidence of this assertion is shown in Fig. 15. Here, intensity cross-correlation traces are shown for two different output slit positions separated by 2-mm transverse distance, as well as two different pixelation mask patterns. The 2-mm transverse distance between the output slit positions corresponds to a 3.6-nm shift in the center wavelength of the output power spectra. The left two traces correspond to the pixelation mask used to measure the power spectra shown in Fig. 14—a periodic 20-pixel "pulse train" mask. The right two traces correspond to a "data packet" mask similar to the mask used for the data presented in Fig. 6. These four cross-correlations clearly show the invariant nature of the output temporal intensity profile as expected from (42) and the recorded power spectra.

VI. Conclusion

The DST pulse shaper has been explored both theoretically and experimentally. The space–time scaling is related to the dispersion and astigmatism of the diffraction grating used in the pulse shaper. The direct scaling between input spatial profile and output temporal intensity profile may prove advantageous for applications in optical communications or photonic A/D conversion. The output chirp of the apparatus, of particular importance for high bit-rate optical communications systems, may be controlled or compensated by a simple geometrical change in the component placement of the apparatus without altering the output temporal intensity profile. Also, multiple spatially separated output channels may be generated simultaneously by utilizing a multiple-slit element at the apparatus output. This feature of the DST apparatus could be of benefit to WDM optical communications, or the generation of multiple, synchronized, but wavelength shifted, pulse trains for high-rate sampling in photonic A/D.

References

[1] A. M. Weiner, J. P. Heritage, and E. M. Kirschner, "High-resolution femtosecond pulse shaping," *J. Opt. Soc. Amer. B*, vol. 5, pp. 1563–1572, 1988.

[2] A. M. Weiner, D. E. Leaird, J. S. Patel, and J. R. Wullert, "Programmable shaping of femtosecond pulses by use of a 128-element liquid-crystal phase modulator," *IEEE J. Quantum Electron.*, vol. 28, pp. 908–920, 1992.

[3] A. M. Weiner, "Femtosecond optical pulse shaping and processing," *Prog. Quantum Electron.*, vol. 19, no. 3, pp. 161–238, 1995.

[4] ——, "Femtosecond pulse shaping using spatial light modulators," *Rev. Sci. Instr.*, vol. 71, pp. 1929–1960, 2000.
[5] M. M. Wefers and K. A. Nelson, "Generation of high-fidelity programmable ultrafast optical waveforms," *Opt. Lett.*, vol. 20, pp. 1047–1049, 1995.
[6] M. A. Dugan, J. X. Tull, and W. S. Warren, "High resolution acousto-optic shaping of unamplified and amplified femtosecond laser pulses," *J. Opt. Soc. Amer. B*, vol. 14, no. 9, pp. 2348–2358, 1997.
[7] D. Yelin, D. Meshulach, and Y. Silberberg, "Adaptive femtosecond pulse compression," *Opt. Lett.*, vol. 22, no. 23, pp. 1793–1795, 1997.
[8] A. Assion, T. Baumert, M. Bergt, T. Brixner, B. Kiefer, V. Seyfried, M. Strehle, and G. Gerber, "Control of chemical reactions by feedback-optimized phase-shaped femtosecond laser pulses," *Science*, vol. 282, pp. 919–922, 1998.
[9] C. J. Bardeen, V. V. Yakovlev, K. R. Wilson, S. D. Carpenter, P. M. Weber, and W. S. Warren, "Feedback quantum control of molecular electronic population transfer," *Chem. Phys. Letters*, vol. 280, pp. 151–158, 1997.
[10] S. Shen and A. M. Weiner, "Complete dispersion compensation for 400-fs pulse transmission over 10-km fiber link using dispersion compensating fiber and spectral phase equalizer," *IEEE Photon. Technol. Lett.*, vol. 11, pp. 827–829, 1999.
[11] H. P. Sardesai, C.-.C Chang, and A. M. Weiner, "A femtosecond code-division multiple-access communication system testbed," *J. Lightwave Technol.*, vol. 16, pp. 1953–1964, 1998.
[12] T. Kurokawa, H. Tsuda, K. Okamoto, K. Naganuma, H. Takenouchi, I. Inoue, and M. Ishii, "Time-space conversion optical signal processing using arrayed waveguide grating," *Electron. Lett.*, vol. 33, pp. 1890–1891, 1997.
[13] H. Tsuda, K. Okamoto, T. Ishii, K. Naganuma, Y. Inoue, H. Takenouchi, and T. Kurokawa, "Second- and third-order dispersion compensator using a high-resolution arrayed-waveguide grating," *IEEE Photon. Technol. Lett.*, vol. 11, pp. 569–571, 1999.
[14] B. Colombeau, M. Vampouille, and C. Froehly, "Shaping of short laser pulses by passive optical Fourier techniques," *Opt. Commun.*, vol. 19, pp. 201–204, 1976.
[15] P. Emplit, J. P. Hamaide, F. Reynaud, C. Froehly, and A. Barthelemy, "Picosecond steps and dark pulses through nonlinear single mode fibers," *Opt. Commun.*, vol. 62, pp. 374–379, 1987.
[16] C. Froehly, B. Colombeau, and M. Vampouille, "Shaping and analysis of picosecond light pulses," in *Progr. Opt.*, E. Wolf, Ed., 1983, vol. 20, p. 65.
[17] P. Emplit, J.-P. Hamaide, and F. Reynaud, "Passive amplitude and phase picosecond pulse shaping," *Opt. Lett.*, vol. 17, pp. 1358–1360, 1992.
[18] D. E. Leaird and A. M. Weiner, "Femtosecond optical packet generation via a direct space-to-time pulse shaper," *Opt. Lett.*, vol. 24, pp. 853–855, 1999.
[19] ——, "Chirp control in the direct space-to-time pulse shaper," *Opt. Lett.*, pp. 850–852, 2000.
[20] O. E. Martinez, "3000 times grating compressor with positive group velocity dispersion: Application to fiber compensation in 1.3–1.6 μm region," *IEEE J. Quantum Electron.*, vol. QE-23, p. 59, 1987.
[21] O. Martinez, "Grating and prism compressors in the case of finite beam size," *J. Opt. Soc. Amer. B*, vol. 3, pp. 929–934, 1986.
[22] M. Wefers and K. A. Nelson, "Space-time profiles of shaped ultrafast optical waveforms," *IEEE J. Quantum Electron.*, vol. 32, pp. 161–172, 1996.
[23] J. W. Goodman, *Introduction to Fourier Optics*. New York: McGraw-Hill, 1968.
[24] J.-C. Diels and W. Rudolph, *Ultrashort Laser Pulse Phenomena*. New York: Academic, 1996.
[25] R. L. Morrison, S. L. Walker, and T. J. Cloonan, "Beam array generation and holographic interconnections in a free-space optical switching network," *Appl. Opt.*, vol. 32, pp. 2512–2518, 1993.
[26] K. Okamoto, "Recent progress of integrated optics planar lightwave circuits," *Opt. Quant. Elec.*, vol. 31, pp. 107–129, 1999.
[27] D. E. Leaird, A. M. Weiner, S. Shen, A. Sugita, S. Kamei, M. Ishii, and K. Okamoto, "High repetition rate femtosecond WDM pulse generation using direct space-to-time pulse shapers and arrayed waveguide gratings," Opt. Quant. Elec., Special Issue on Components for Ultrafast Commun., to be published.
[28] A. Yariv, *Optical Electronics*. Philadelphia, PA: Saunders, 1991.
[29] J. T. Verdeyen, *Laser Electronics*. Englewood Cliffs, NJ: Prentice-Hall, 1995.
[30] S. Ramo, J. R. Whinnery, and T. Van Duzer, *Fields and Waves in Communications Electronics*. New York: Wiley, 1994.

Daniel E. Leaird was born in Muncie, IN, in 1964. He received the B.S. degree in physics from Ball State University, Muncie, IN, in 1987, and the M.S. and Ph.D. degrees from the School of Electrical and Computer Engineering, Purdue University, West Lafayette, IN, in 1996 and 2000, respectively.

He joined Bellcore, Red Bank, NJ, as a Senior Staff Technologist, and later became a Member of Technical Staff. From 1987 to 1994, he worked in the Ultrafast Optics and Optical Signal Processing Research Group, where he was a Key Team Member in research projects in ultrafast optics, such as shaping of short optical pulses using liquid-crystal modulator arrays, investigation of dark soliton propagation in optical fibers, impulsive stimulated Raman scattering in molecular crystals, and all-optical switching. He is currently a Research Engineer and Laboratory Manager of the Ultrafast Optics and Optical Fiber Communications Laboratory, Purdue University, where he has been since 1994. He has co-authored approximately 40 journal articles and 50 conference papers. His first U.S. patent is currently pending.

Dr. Leaird has received several awards for his work in the ultrafast optics field, including a Bellcore "Award of Excellence," a Magoon Award for Outstanding Teaching, and an Optical Society of America/New Focus Student Award.

Andrew M. Weiner (S'84–M'84–SM'91–F'95) was born in Boston, MA, in 1958. He received the Sc.D. in electrical engineering from Massachusetts Institute of Technology, Cambridge, in 1984.

During 1979–1984, he was a Fannie and John Hertz Foundation Graduate Fellow at M.I.T. In 1984, he joined Bellcore, Red Bank, NJ, where he conducted research on ultrafast optics, including shaping of ultrashort pulses, nonlinear optics and switching in fibers, and spectral holography. In 1989, he became Manager of the Ultrafast Optics and Optical Signal Processing Research District. In 1992, he began his current position as Professor of Electrical and Computer Engineering, Purdue University, West Lafayette, IN. Since August, 1996, he has also been serving as Director of Graduate Admissions for the School of Electrical and Computer Engineering. He spent the 1999–2000 academic year as a Visiting Professor at the Max Born Institute for Nonlinear Optics and Short Pulse Spectroscopy, Berlin, Germany. His current research interests center on processing of ultrashort pulses, high-speed optical communications, applications of pulse shaping to femtosecond spectroscopy and nonlinear optics, terahertz radiation, and optical imaging in scattering media. He has published four book chapters and approximately 100 journal articles. He has been author or co-author of 200 conference papers, including approximately 60 conference invited talks, and has presented over 50 additional invited seminars at universities or industry. He is the holder of five U.S. patents.

Dr. Weiner has served on, or chaired, numerous research review panels, professional society award committees, and conference program committees. He was General Co-Chair of the 1998 Conference on Lasers and Electro-optics, and Chair of the 1999 Gordon Conference on Nonlinear Optics and Lasers. In 1988–1989, he was selected as an IEEE Lasers and Electro-optics Society (LEOS) Traveling Lecturer. In addition, he has served as Associate Editor for IEEE JOURNAL OF QUANTUM ELECTRONICS, IEEE PHOTONICS TECHNOLOGY LETTERS, and *Optics Letters*. He served as an Elected Member of the Board of Governors of the IEEE Lasers and Electro-Optics Society from 1997–1999, and is currently Secretary/Treasurer of that organization. He was awarded the 1990 Adolph Lomb Medal of the Optical Society of America for pioneering contributions to the field of optics made before the age of 30 and is a Fellow of the Optical Society of America. He was also awarded the Curtis McGraw Research Award of the American Society of Engineering Education (1997), the International Commission on Optics Prize (1997), the IEEE LEOS William Streifer Scientific Achievement Award (1999), and the Alexander von Humboldt Foundation Research Award for Senior U.S. Scientists (2000). His doctoral thesis, for which he was awarded the 1984 Hertz Foundation Doctoral Thesis Prize, dealt with femtosecond pulse compression (including generation of the shortest optical pulses reported up to that time) and measurement of femtosecond dephasing in condensed matter.